

All-Dielectric Silicon Metasurface with Strong Subterahertz Toroidal Dipole Resonance

Dimitrios C. Zografopoulos,* Antonio Ferraro, José Francisco Algorri, Pedro Martín-Mateos, Braulio García-Cámara, Aldo Moreno-Oyervides, Viktor Krozer, Pablo Acedo, Ricardo Vergaz, José Manuel Sánchez-Pena, and Romeo Beccherelli

A single-layer, all-dielectric metasurface exhibiting a strong toroidal resonance in the low-atmospheric loss radio window of the subterahertz W-band is theoretically proposed and experimentally demonstrated. The metasurface is fabricated on a high-resistivity floating-zone silicon wafer by means of a single-process, wet anisotropic etching technique. The properties of the toroidal mode of both the constituent dielectric elements and the metasurface are rigorously investigated by means of the multipole decomposition technique and full-wave simulations. The experimental demonstration of such a compact, all-silicon metasurface opens new venues of research in the investigation of toroidal modes and the engineering of functional millimeter-wave components, which can be scaled to terahertz and higher frequencies of the electromagnetic spectrum.

properties of propagating electromagnetic waves, such as wave front, polarization, intensity, or spectrum, in ways unachievable by bulk materials of the same sub-wavelength thickness.^[1–3] The constituent elements of a metasurface can be either metallic or dielectric and they are usually patterned on a low-loss, dielectric substrate. All-dielectric metasurfaces, in particular, which are composed of elements made of a high-refractive index dielectric material, have been lately attracting more attention, as they show a very high diversity of exploitable properties, while being free from ohmic losses associated with the presence of metals.^[4] The potential

1. Introduction

Metasurfaces are 2D periodic arrays of subwavelength resonant scatterers whose arrangement and interaction can modify the

of dielectric metasurfaces as a platform for low-loss, compact, functional components has been extensively demonstrated in numerous applications, such as reflection/refraction control and wave-front shaping,^[5–8] lensing,^[9] control of light emission^[10,11] or photoluminescence,^[12,13] polarization control^[14,15] and polarimetry,^[16] generation of vortex beams,^[17] highly selective filtering,^[18,19] or enhancement of nonlinear processes.^[20,21]

Dr. D. C. Zografopoulos, Dr. A. Ferraro, Dr. R. Beccherelli
Consiglio Nazionale delle Ricerche
Istituto per la Microelettronica e Microsistemi
Via del fosso del cavaliere 100, 00133 Rome, Italy
E-mail: dimitrios.zografopoulos@artov.imm.cnr.it

Dr. J. F. Algorri, Dr. B. García-Cámara, Dr. R. Vergaz,
Prof. J. M. Sánchez-Pena
Group of Displays and Photonic Applications (GDAF)
Department of Electronic Technology
Carlos III University of Madrid
Madrid 28911, Spain

Dr. P. Martín-Mateos, A. Moreno-Oyervides, Prof. P. Acedo
Sensors and Instrumentation Techniques (SIT)
Department of Electronic Technology
Carlos III University of Madrid
Madrid 28911, Spain

Prof. V. Krozer
Physics Institute
Goethe University Frankfurt am Main
60438 Frankfurt am Main, Germany

 The ORCID identification number(s) for the author(s) of this article can be found under <https://doi.org/10.1002/adom.201900777>.

© 2019 The Authors. Published by WILEY-VCH Verlag GmbH & Co. KGaA, Weinheim. This is an open access article under the terms of the Creative Commons Attribution-NonCommercial License, which permits use, distribution and reproduction in any medium, provided the original work is properly cited and is not used for commercial purposes.

The copyright line was changed on 13 August 2019 after initial publication.

DOI: 10.1002/adom.201900777

In addition to offering novel solutions in practical applications, metasurfaces can also provide insight in theoretical physics, optics, and the investigation of phenomena based on particular light–matter interaction conditions. One such case is that of toroidal modes, which have been under intense investigation, thanks to their unusual electromagnetic properties. The toroidal dipole, the simplest toroidal mode, is generated by a current flowing in a solenoid, which is bent into a torus. Under certain conditions, the excitation of the toroidal dipole can interfere destructively with the electric dipole mode and cancel the far-field scattering radiation of dielectric particles, in the so-called “anapole” state.^[22]

Since decades ago, toroidal modes were employed in physics, for instance, to explain the parity violation of the weak interactions in atomic nuclei,^[23] to propose models of stable atoms,^[24] or to describe dark matter.^[25] In recent years, though, the interest on electromagnetic toroidal moments is rapidly increasing as, apart from the fundamental physical insight, they can be harnessed in numerous applications.^[26,27] Toroidal modes in individual dielectric particles or small clusters have been theoretically proposed for the excitation of toroidal response,^[28] cloaking,^[29] enhanced absorption,^[30] and nanolasing^[31] or experimentally demonstrated as nonradiating sources^[32] and for the enhancement of nonlinear effects.^[33,34] Moreover, it

has been shown that enhanced toroidal resonances, which do not manifest in natural materials, can be observed and tailored thanks to the engineering possibilities offered by metasurfaces. Indeed, numerous studies have been conducted lately, either targeting the investigation itself of toroidal resonances,^[35,36] or the exploitation of their properties in applications such as beam steering,^[37] cross-polarization conversion,^[38] and the design of high-quality factor resonators.^[36,39–42]

Nevertheless, there are only very few experimental demonstrations of dielectric metasurfaces that produce a strong toroidal resonant response. A first demonstration employed a periodic arrangement of tubes of water in a dielectric background, which exhibited a toroidal dipolar response in the low-GHz frequency range, thanks to the high permittivity of water.^[43] Recently, two types of metasurfaces with a toroidal response in the vicinity of 10 GHz have been demonstrated, based on the periodic arrangement of subwavelength dielectric bars or disks embedded in a low-permittivity matrix.^[44,45] In this work, a not yet explored approach for the design and fabrication of all-dielectric toroidal metasurfaces is presented. The metasurface is fabricated by a single step of wet anisotropic etching of a high-resistivity floating-zone silicon (HRFZ-Si) wafer with appropriately selected thickness. The metasurface design is based on the investigation of the scattering properties of the constituent elements, by means of the multipole decomposition method, and the study of the metasurface electromagnetic response via full-wave simulations of the finite-element method. A resonant toroidal dipole mode is experimentally observed at approximately 92.5 GHz, consistent with the theoretical design, which focused on the 92–95 GHz atmospheric radio window of the subterahertz W-band, with an eye on applications including 5G-and-beyond wireless communications, satellite and radar links.

This first demonstration is a proof-of-concept for the experimental excitation and characterization of toroidal modes and the design of compact components in the W-band, based on the manipulation of electromagnetic waves via strong toroidal resonances. Instead of relying in assembling clusters of dielectric particles embedded in a dielectric support medium, the proposed technique involves a single photolithographic step and a standard self-stopping wet etching procedure that starts from a planar HRFZ-Si wafer and results in a monolithic, single-piece component that can be replicated in large volumes at low cost. The metasurface is mechanically supported by a deeply subwavelength residual silicon bottom layer, hence eliminating the need for embedding the dielectric elements in an additional dielectric matrix. Thanks to the very low material dispersion of silicon, the same structure can be directly scaled to higher frequencies using the same etching technique, by employing commercially available thinner HRFZ-Si substrates. Finally, such all-silicon metasurfaces can also potentially exhibit tunable properties, e.g., via the optical excitation of carriers, which can drastically modify the conductivity of silicon.

2. Anapole States in Dielectric Prismatic Elements

The metasurface design is based on an idealized dodecagonal prismatic element (DPE) depicted in Figure 1a. This particular

geometry was selected as the constituent element, as it closely approximates the employed fabrication process, as it will be discussed in detail in Section 4. The two bases of the DPE are regular dodecagons with total width equal to W and w for the bottom and top surfaces respectively, as defined in Figure 1a. The walls are slanted at an angle $\theta = 54.7^\circ$, which corresponds to half the value between the sp^3 hybridized Si–Si single bonds, as dictated by the wet etching process of the (100) planes in alkali solutions. This process is nearly self-stopping thanks to the much slower etching rate of denser crystallographic planes, such as the exposed $\langle 111 \rangle$ oriented planes. In real experimental conditions, when no compensation techniques are employed further planes are exposed in the process, resulting in structures very closely approximated by DPE. By

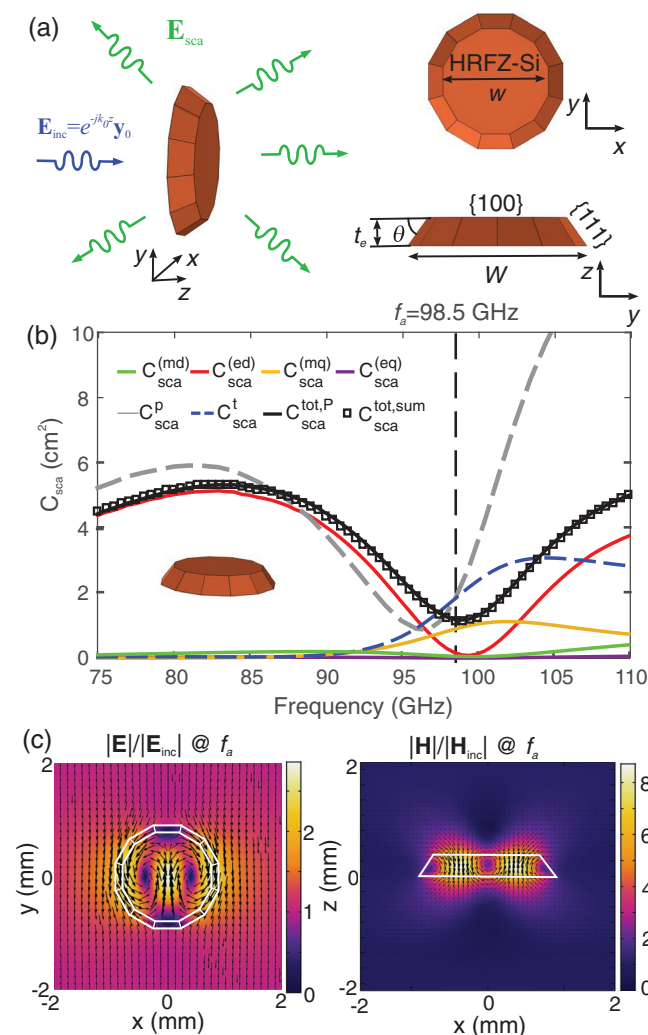


Figure 1. a) Schematic layout of the investigated dodecagonal prismatic element made of HRFZ-Si and the definition of the scattering problem. The angle $\theta = 54.7^\circ$ corresponds to anisotropic wet etching of silicon in alkaline solution. b) Multipole decomposition and scattering cross-sections for the dipole and quadrupole modes supported by the dielectric element for $W = 1.8$ mm, $w = 1.404$ mm, and $t_e = 0.28$ mm. c) Electric and magnetic field profiles at the $z = t_e/2$ and $y = 0$ planes, respectively, calculated at the anapole frequency $f_a = 98.5$ GHz. The characteristic electric and magnetic line distributions of the anapole state are evidenced.

simple trigonometry, the dimensions of the DPE are connected via the relation

$$W = w + 2 \frac{t_e}{\tan \theta} \quad (1)$$

where t_e is the DPE thickness.

The DPE is irradiated with a planewave that propagates along the z -axis, namely the short axis of the DPE, and linearly polarized along the y -axis, with reference to the coordinate system of Figure 1a. The surrounding medium is air and the dimensions of the DPE are $W = 1.8$ mm, $t = 0.28$ mm, and $w = 1.404$ mm. The refractive index of HRFZ-Si in this spectral range is $n_{\text{Si}} = 3.416$.

The electric field $\mathbf{E}(\mathbf{r})$ in the DPE is calculated by employing the scattered-field formulation in the finite-element method implemented in the commercial software COMSOL Multiphysics. Subsequently, the multipole decomposition method in Cartesian coordinates is employed,^[41,42,46] in order to calculate the individual contributions of the electric dipole (ed), electric quadrupole (eq), magnetic dipole (md), and magnetic quadrupole (mq) moments to the total scattering cross-section $C_{\text{sca}}^{\text{tot}}$ of the DPE. Moreover, the separate contributions of the Cartesian electric dipole (p) and toroidal dipole (t) moments are also calculated, since the crossing point of their respective cross-section spectra $C_{\text{sca}}^{\text{p}}$ and $C_{\text{sca}}^{\text{t}}$ provides an indication of the anapole frequency.

Finally, we calculate the total scattering cross-section $C_{\text{sca}}^{\text{tot,P}}$ of the DPE by integrating the outgoing power flow over the element's surface, normalized to the energy flux of the incident wave P_{in}

$$C_{\text{sca}}^{\text{tot,P}} = \frac{1}{P_{\text{in}}} \int_S \mathbf{n} \cdot \mathbf{P}_{\text{sca}} dS \quad (2)$$

where \mathbf{P}_{sca} is the Poynting vector of the scattered field and $P_{\text{in}} = 0.5 |\mathbf{E}_{\text{inc}}|^2 / Z_0$, where Z_0 is the characteristic impedance of vacuum and $|\mathbf{E}_{\text{inc}}| = 1 \text{ V m}^{-1}$ is the amplitude of the impinging electric field.

Figure 1b shows the calculated cross-section spectra in the investigated frequency window. The total scattering cross-section $C_{\text{sca}}^{\text{tot,P}}$ coincides with $C_{\text{sca}}^{\text{tot,sum}}$, namely the sum of the four individual contributions

$$C_{\text{sca}}^{\text{tot,sum}} = C_{\text{sca}}^{\text{(ed)}} + C_{\text{sca}}^{\text{(md)}} + C_{\text{sca}}^{\text{(eq)}} + C_{\text{sca}}^{\text{(mq)}} \quad (3)$$

thus demonstrating that the contribution of higher order multipoles is negligible. The frequency f_a where the anapole state manifests is identified by the crossing of $C_{\text{sca}}^{\text{p}}$ and $C_{\text{sca}}^{\text{t}}$, which is accompanied by the cancellation of the far-field scattering of the electric dipole ($C_{\text{sca}}^{\text{(ed)}}$). The total scattering cross-section is minimized at f_a , the only nonvanishing contribution being that of the magnetic quadrupole mode.

The excitation of the anapole state is further corroborated by examining the electric and magnetic field profiles at the $z = t/2$ and $y = 0$ planes, respectively, at the anapole frequency $f_a = 98.5$ GHz, as depicted in Figure 1c. Two opposite loops of displacement currents are observed in the two sides of the DPE, which generate a circular magnetic moment distribution vertical to the disk surface. Such distribution

provides a strong circular toroidal moment oriented parallel to the DPE's surface.^[22] The calculated field profiles show a field enhancement factor of almost 3 for the electric and 9 for the magnetic field, with respect to the amplitudes of the impinging planewave.

3. All-Dielectric Metasurfaces with Strong Toroidal Dipole Resonance

The investigated metasurface is composed of a square periodic array of DPE, as illustrated in Figure 2a. The dimensions of the DPE are the same ones considered in the analysis of the properties of the single DPE in Section 2. The elements are patterned on a single HRFZ-Si wafer whose total thickness is $t_w = 300 \mu\text{m}$. The lattice pitch of the array p is defined by the width W of the DPE ($p = W$), as in the unit cell shown in Figure 2a. The wafer thickness is higher than the total etching depth, which coincides with the DPE thickness t_e . In this way, a residual HRFZ-Si remains with thickness $t_s = t_w - t_e = 20 \mu\text{m}$. Thus, the metasurface is formed by a single process of wet anisotropic etching of the HRFZ-Si, while the residual layer provides the basis and mechanical support of the DPE array. The thickness t_s is deeply subwavelength and it was found to have a negligible effect in the metasurface properties. Overall, the dimensions of the structure were selected such that the anapole state of the DPE manifests within the frequency range of interest, namely the

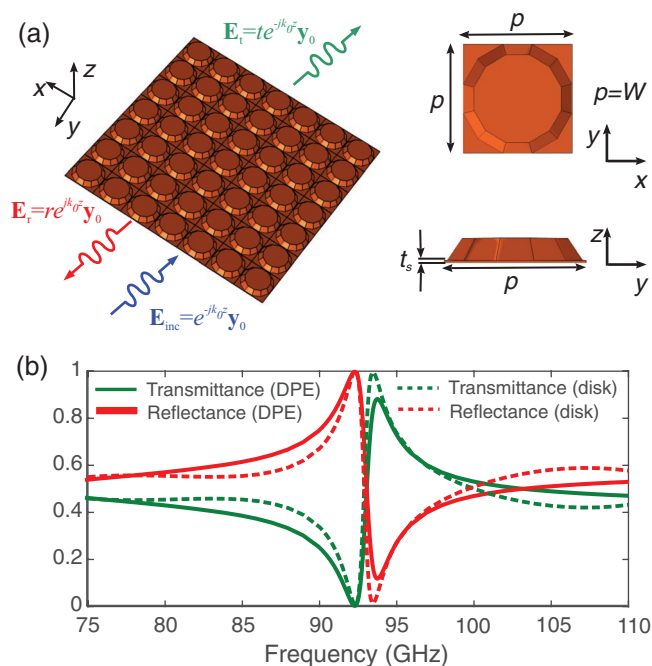


Figure 2. a) Schematic layout of the investigated metasurface, composed of a square array of dodecagonal prismatic elements patterned on a single HRFZ-Si substrate of thickness $300 \mu\text{m}$. The thickness of the HRFZ-Si residual layer is $t_s = 20 \mu\text{m}$ and the pitch equals the base of the DPE ($p = W$). Other geometrical parameters as in Figure 1. b) Theoretically calculated power transmittance and reflectance spectra of the metasurface. The dashed lines are reference spectra corresponding to a metasurface of the same pitch with disk elements of the same thickness t_e and radius $r_d = 0.82$ mm.

W-band (75–110 GHz), and particularly the low-atmospheric loss window between 92 and 95 GHz.

The structure is irradiated with a γ -polarized planewave impinging perpendicularly on the metasurface. The lattice pitch of $p = W = 1.8$ mm is less than half of the wavelength in the whole investigated spectral range and, consequently, no propagating diffraction orders are allowed. The transmission and reflection properties of the metasurface are described via the field transmission complex coefficients t and r , respectively. Figure 2b shows the power transmittance T and reflectance R spectra of the metasurface, defined as $T = |t|^2$ and $R = |r|^2$.

A single resonance at $f_t = 93.2$ GHz with a characteristic asymmetric Fano lineshape is observed in the frequency window under investigation. Figure 2 also shows a pair of reference spectra, which correspond to an HRFZ-Si metasurface with the same pitch p and layer thicknesses (t_s , t_c), but employing disks instead of DPE. The disk radius was $r = 0.82$ mm, such that the volumes of the disk and DPE are approximately the same. The response of the reference metasurface shows the same qualitative features, namely resonant frequency and the asymmetric lineshape, thus demonstrating the suitability of the proposed fabrication technique for the excitation of the toroidal response. In fact, it has been demonstrated that strong toroidal resonances can manifest in various shapes of dielectric particles, cuboids for instance,^[30,42,46] the critical parameter being the particle's aspect ratio and not the shape itself.^[22,30,33]

In order to elucidate on the nature of the observed resonance, the multipole decomposition technique is repeated for the fields calculated in the unit cell of the metasurface. The relative contributions of the dipole and quadrupole modes are plotted in Figure 3a. Strong maxima are observed at $f_t = 93.2$ GHz for the total electric dipole mode, which stem from the excitation of the toroidal dipole mode. The anapole frequency lies on the high-frequency side of the resonance, at 95.6 GHz.

These results provide insight on the nature of the excited resonance at f_t , which is fundamentally toroidal, as further evidenced by the electric and magnetic field profiles shown in Figure 3b. The corresponding field enhancement factors for the electric and magnetic fields are 11 and 30, respectively, namely four times larger than those calculated at the anapole frequency of the single DPE. It is known that in a metasurface configuration the radiative damping can be reduced thanks to collective oscillations mediated by near-field coupling between the constituent particles and the supported multipole modes.^[18,47] In the investigated example the periodic arrangement of the DPE produces strong resonances with a prominent toroidal dipole mode contribution, which was targeted in the design of the metasurface.

4. Experimental Demonstration of a Silicon Metasurface with Sub-THz Toroidal Resonances

4.1. Fabrication

The metasurface was fabricated on a 2 in., double-side polished HRFZ-Si wafer with $(100) \pm 0.5^\circ$ orientation, whose thickness was measured to be $t_w = 300 \pm 5$ μm (the nominal total thickness

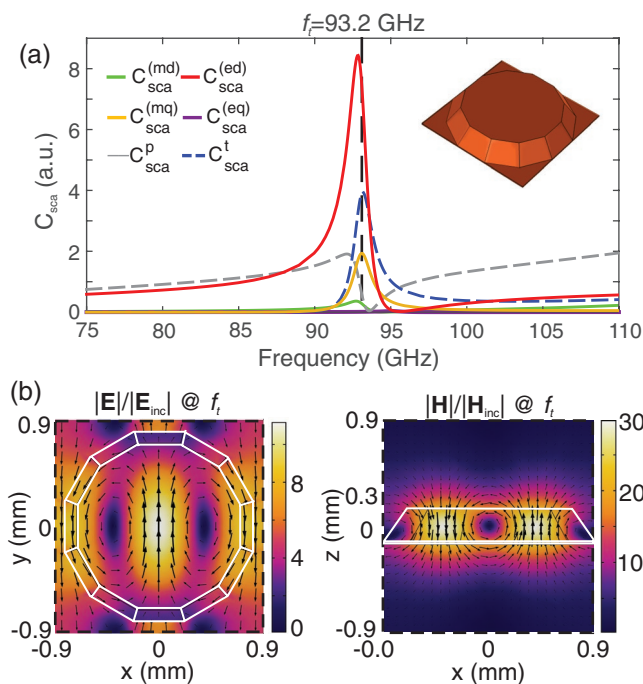


Figure 3. a) Scattering efficiency of the dipolar and quadrupolar multipole modes, calculated in the unit cell of the metasurface studied in Figure 2, showing a strong toroidal dipole resonance at $f_t = 93.2$ GHz. b) Electric and magnetic field profiles at the $z = t/2$ and $y = 0$ planes of the unit cell, respectively, calculated at the toroidal resonant frequency f_t .

variation was below 10 μm). The silicon resistivity declared by the manufacturer is higher than 10 $\text{k}\Omega$ cm (Siltronix). A standard KOH wet anisotropic etching process was employed. First, the wafer was cleaned with an $\text{H}_2\text{SO}_4:\text{H}_2\text{O}_2$ solution at a ratio of 1:1, followed by HF for 30 s and rinsed with deionized water. Then, it was placed in an oxidation furnace for ≈ 48 h, which yielded a SiO_2 buffer layer of ≈ 2 μm thickness. A film with thickness 1.3 ± 0.1 μm of the photoresist S1813 (Shipley) was spin-coated on both sides of the wafer at 4000 rpm for 60 s and then cured at 115 $^\circ\text{C}$ for 120 s.

The photolithography was carried out using a Karl Suss MA150 mask aligner ($\lambda = 365$ nm, $I = 60$ mW cm^{-2}). The mask was aligned such that the square metasurface side was parallel to the $\langle 110 \rangle$ oriented cut of the wafer. Subsequently, the sample was immersed in the photoresist developer MF319 for 50 s, rinsed with deionized water and dried with nitrogen. The exposed SiO_2 parts were etched away with buffered HF at an etch rate of 100 nm min^{-1} and the residual resist was removed with acetone and isopropanol.

Then, the sample was fixed in a wafer holder and placed in a glass container with a KOH 4 M solution at 80 $^\circ\text{C}$. A magnetic stirrer was used to remove the hydrogen bubbles resulting from the etching reaction. The etching rate was estimated at circa 1 $\mu\text{m min}^{-1}$ and the sample was removed after ≈ 4.5 h. The etching resulted in the formation of a square periodic array of 7×7 prismatic elements, for a total surface of 1.26×1.26 cm^2 , as shown in Figure 4a.

The photolithographic mask, shown in Figure 4b, was composed of a periodic lattice ($p = 1.8$ mm) of squares

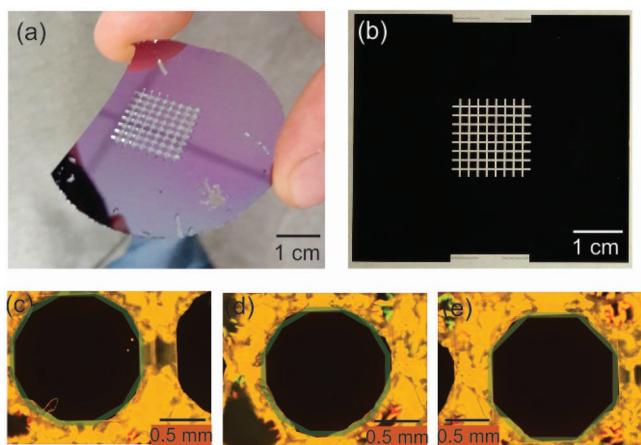


Figure 4. a) Photograph of the fabricated sample, showing a square periodic array of 7×7 prismatic elements, for a total surface of $1.26 \times 1.26 \text{ cm}^2$, patterned on a single HRFZ-Si wafer via anisotropic wet etching. b) The mask used for the etching of the wafer. c–e) Microscope images of selected prismatic elements showing clear convex corner undercutting, with respect to the square profile of the mask. The elements' cross-section shape can be fitted with good accuracy to regular dodecagons or octagons.

$1.404 \times 1.404 \text{ mm}^2$ in size. It is well known that the etching in alkali solution of $\langle 100 \rangle$ oriented silicon wafers protected by a crystallographically aligned square or rectangular SiO_2 mask results in convex corner undercutting unless compensation techniques are employed.^[48] In our specific case, the undercutting is intentionally exploited to produce dodecagonal or octagonal features. Typical results obtained by the employed process are illustrated in the microscope micrographs of Figure 4c–e. The shape of the resulting prismatic elements is close to a disk, namely the archetype for the investigation of toroidal modes.

The morphological inspection of the sample under optical microscope reveals some degree of irregularity with respect to the shape of the etched elements and the overall geometric parameters, e.g., etching depth, as demonstrated in Figure 4c–e. Therefore, although the periodicity of the array, as defined by photolithography, was preserved, the geometry of the individual elements shows some distribution, which led to the spectral broadening of the measured spectra, as it will be discussed in Section 4.3.

4.2. Characterization

The characterization of the sample was conducted by means of a millimeter-wave spectroscopic instrument working in the W-band, which is tuned from 75 to 110 GHz in steps of 1.5 GHz. The simplified block diagram and image of the setup can be found in Figure 5. The main parts/components are labeled with numbers. In particular, Part #1 is an AFM6-110 Active Frequency Multiplier (Radiometer Physics GmbH, Meckenheim, Germany) with a multiplication factor of six and a frequency range from 75 to 110 GHz, which is employed in the generation of the high frequency signal that is directly coupled into a WR10 waveguide.

A directional coupler (Part #3) is used together with an HMR-110-6W-band receiver (Part #2) (Radiometer Physics GmbH, Meckenheim, Germany) to obtain a reference measurement of the generated signal. The sample is positioned between the exciting and receiving ports (Parts #4 and #6). An additional HMR-110-6 receiver (Part #7) is employed to measure the signal transmitted through the sample (Part #5). The radio frequency and local oscillator signals needed for the generation of the mm-wave radiation are swept between 12.5 and 18.5 GHz in steps of 250 MHz using APSYN420 (AnaPico,

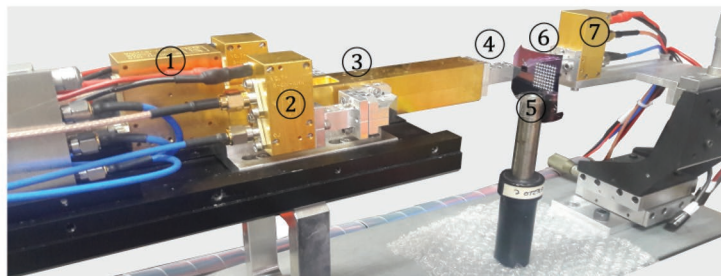
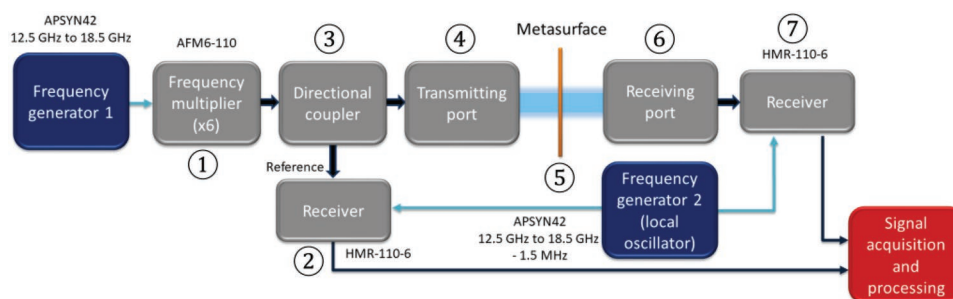


Figure 5. Block diagram of the microwave system for the characterization of the metasurface in the W-band and photo of the measurement setup.

Zurich, Switzerland) synthesizer. To avoid the saturation of the receivers, the setup is supplemented with switchable attenuators, which adjust the input power to the frequency multiplier and the receivers at each frequency setting.

For the acquisition of the signals a frequency offset of 1.5 MHz is set between the AFM6-110 Frequency Multiplier and the local oscillator frequency of the W-band receiver producing a 9 MHz intermediate frequency for the signals in the 75–110 GHz frequency range. The 9 MHz intermediate frequency output signals for the reference, reflection and transmission channels are directly sampled at 10 MHz by an acquisition card (Handyscope HS4-10, TiePie engineering, Sneek, Netherlands) and processed using LabView. The program, running in real-time and working as a multichannel lock-in amplifier, was designed to obtain the amplitudes of the signals reaching the receivers and the phase difference between the reference signal and the transmitted signal.

4.3. Results and Discussion

Figure 6 shows a comparison between the measured and numerically calculated spectra for the transmitted power $T = |t|^2$ and phase ϕ ($\phi = \angle t$) of the metasurface, where t is the field transmission coefficient as defined in Section 3. The transmittance of the HRFZ-Si slab, measured on a uniform (nonpatterned) area of the same wafer is also included in Figure 6a. The simulations of the DPE metasurface, as investigated in Section 3, were repeated for a metasurface composed of octagonal prismatic elements (OPE) of the same width W and thickness t_e . Since the OPE volume is slightly larger than that of the DPE (0.6 vs 0.58 mm³), the corresponding resonance f_t is shifted toward lower frequencies by 0.8 GHz. However, the shape of the transmitted power and phase spectra is essentially the same in both cases, apart from the observed frequency shift. In order to estimate the quality factor Q of the resonance, we fitted the calculated transmittance spectrum for the OPE metasurface to the Fano formula^[49]

$$T(\omega_n) = C \frac{(F\gamma_n + \omega_n - 1)^2}{(\omega_n - 1)^2 + \gamma_n^2} \quad (4)$$

where $\omega_n = \omega/\omega_0$ is the normalized angular frequency, $\omega_0 = 2\pi f_t$, γ_n describes the normalized linewidth of the resonance, F is the Fano parameter, expressing the degree of asymmetry, and C is a normalization constant. The resulting fitting parameters were found equal to $C_1 = 0.4397$, $\gamma_n = 7.18 \times 10^{-3}$, and $F = 0.9583$ and the quality factor is calculated as $Q = 1/\gamma_n = 139$.

The measured spectra show a clear broadening, consistent in power transmittance and phase, with respect to the simulated results. The OPE spectra are positioned approximately at the center of the measured resonances, which can be attributed to the fact that the OPE volume is close to the average volume of the fabricated elements. Apart from the broadening though, the Fano-like shape of the measured resonance spectra, both in terms of power and phase, agrees with the theoretical simulations. Such agreement, together with the multipole analysis of Section 3, which constitutes the standard tool for the identification of the multipolar nature of

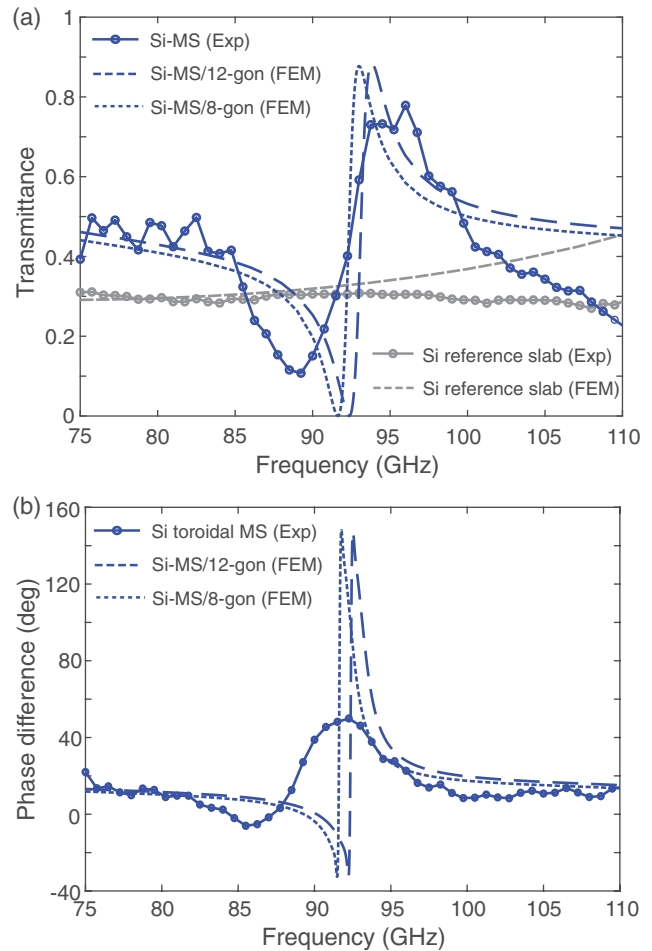


Figure 6. Measured and calculated spectra of the transmitted a) power and b) phase of the investigated metasurface. The power transmittance of the nonpatterned HRFZ-Si slab is also shown in (a). The numerical results were performed assuming dodecagonal and octagonal prismatic elements. Significant broadening of the experimentally measured spectra is observed.

metasurface resonances,^[39,43,44] corroborates the observation of a resonant toroidal dipole response of the experimentally characterized metasurface.

A first candidate that could account for the observed spectral broadening is carrier-induced absorption losses in silicon. Taking the worst-case, low-resistivity limit for the intrinsic HRFZ-Si wafer, namely $\rho = 10$ k Ω cm, the carrier concentration can be calculated as $n_c = [\rho q_e(\mu_e + \mu_h)]^{-1} \approx 3.4 \times 10^{11}$ cm⁻³, where $q_e = 1.6 \times 10^{-19}$ C is the electron charge and $\mu_e = 1400$ cm² V⁻¹ s⁻¹ and $\mu_h = 450$ cm² V⁻¹ s⁻¹ are the electron and hole mobility for silicon, respectively. Next, we consider a Drude model for the permittivity of silicon

$$\epsilon_{\text{Si}} = \epsilon_o \left(1 - \frac{\omega_p^2}{\omega^2 - j\gamma\omega} \right) \quad (5)$$

where $\epsilon_o = n_{\text{Si}}^2 = 11.67$ accounts for the background polarizability of silicon, ω_p is the plasma frequency, and γ the damping rate, given, respectively by

$$\omega_p = \sqrt{\frac{n_e q_e^2}{\epsilon_0 \epsilon_0 m_e^*}}, \text{ and } \gamma = \frac{q_e}{\mu_e m_e^*} \quad (6)$$

where $\epsilon_0 = 8.854 \times 10^{-12}$ F/m is the free-space permittivity and $m_e^* = 1.08 m_e$ is the effective electron mass with $m_e = 9.11 \times 10^{-31}$ kg being the electron mass. The resulting plasma frequency $f_p = \omega_p/2\pi$ and damping rates are $f_p = 1.47$ GHz and $\gamma_f = \gamma/2\pi = 185$ GHz. Thus, at the frequency of 100 GHz, the complex permittivity of HRFZ-Si is $\epsilon_{Si} = 11.67(1 - j9 \times 10^{-5})$, which is consistent with what reported in the literature for resistivity values equal to the one here considered.^[50] Such values for the loss tangent ($\tan \delta = 9 \times 10^{-5}$), which are much lower than most dielectric materials used in microwave technology, confirm the suitability of HRFZ-Si for the design of the proposed metasurfaces. In principle, the effect of this small amount of dielectric losses could be noticeable in structures with very high-Q resonances. In order to clarify this point, the simulation of the electromagnetic response of the OPE metasurface was repeated by introducing the Drude model for the Si permittivity, as defined in Equation (5). The results are shown in Figure 7a, revealing an almost negligible effect. A maximum power absorption of 2% at the resonant frequency and a maximum deviation of 5° in the phase of the transmitted wave were calculated. Therefore, dielectric losses can be excluded as the cause of the observed broadening.

In order to further elucidate the nature of the resonance broadening in the measured spectra, we resort to an approximate interpretation based on a weighted average of the simulated spectra. This approach accounts for the observed nonuniformity of the fabricated prismatic element shape due to, for instance, slightly diverse etching rates of the planes exposed in different elements or small variations of the etching angle, which is often found to deviate from the theoretical value of 54.7° during the etching of convex angles.^[51]

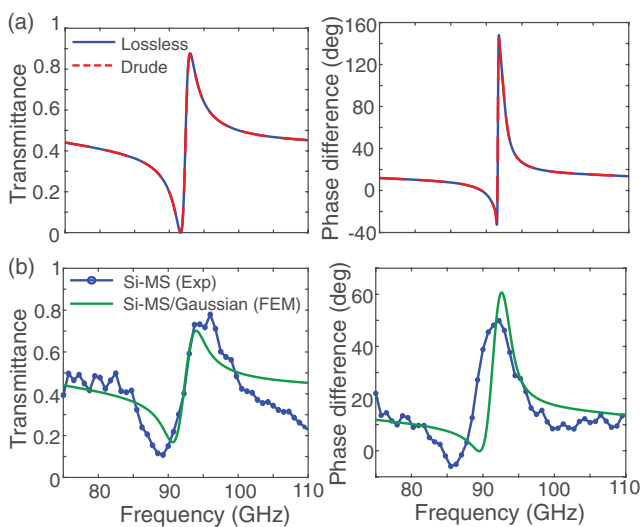


Figure 7. a) Comparison of the reference simulated metasurface spectra with those corresponding to the case of Drude permittivity for HRFZ-Si (Equation (5)). b) Comparison of the experimentally measured spectra with the weighted averaged spectra (Equation (8)).

Such resonance spectral broadening is a well-known phenomenon in metasurfaces due to variations of, e.g., lattice dimensions,^[52] size distribution in colloidal nanoparticle self-assembled arrays^[53] or, as in this case, the resonator shape.^[54] First, the OPE power and phase spectra, $T^{\text{OPE}}(f)$ and $\phi^{\text{OPE}}(f)$, are taken as reference. Next, we consider that the variation of the fabricated elements' shape is such that the spectra of the metasurfaces corresponding to each slightly different geometry are shifted by f_d with respect to the reference ones, i.e., $T(f) = T^{\text{OPE}}(f - f_d)$ and $\phi(f) = \phi^{\text{OPE}}(f - f_d)$. A Gaussian distribution is employed for the frequency shift f_d with a standard deviation of $\sigma = 1$ GHz, namely

$$p(f_d) = \frac{1}{\sqrt{2\pi}} e^{-\frac{f_d^2}{2}} \quad (7)$$

The averaged spectrum, e.g., for the power transmittance, is then calculated as

$$\bar{T}(f) = \frac{\int_{f_1-f_0}^{f_2-f_0} p(f_d) T^{\text{OPE}}(f - f_d) df_d}{\int_{f_1-f_0}^{f_2-f_0} p(f_d) df_d} \quad (8)$$

where $f_1 = 75$ GHz, $f_2 = 110$ GHz, and $f_0 = 92.4$ GHz is the toroidal dipole resonant frequency of the OPE metasurface. The averaged phase spectrum is calculated in an analogous manner. The resulting calculated averaged spectra are shown in comparison with the experimental measurements in Figure 7b. A high degree of agreement is observed, particularly in terms of the resonance linewidth, which indicates that the measured spectral broadening can be attributed to the nonhomogeneity of the sample geometry. Hence, sharper spectral features in agreement with numerical results are expected by using more expensive fabrication techniques, such as deep reactive ion etching.^[55]

Given the very low material dispersion of silicon, the scaling of the proposed metasurface to higher frequencies is straightforward by reducing the HRFZ-Si wafer thickness and correspondingly the dimensions of the unit cell and metasurface periodicity. Since these dimensions are defined by the photolithographic mask, the design can be theoretically scaled up to the near-infrared spectrum, before the onset of silicon absorption at approximately 1.1 μm . One practical limit in up-scaling is the availability of thin HRFZ-Si wafers. Thicknesses down to 50 μm are commercially available,^[56] which would shift the investigated toroidal resonance to approximately 550 GHz. Further scaling would be limited by the availability and also the handling of very thin HRFZ-Si wafers. However, in case the metasurface is patterned on a low index substrate, e.g., silica, the device operation can be scaled up to the near-infrared spectrum, provided the effect of the substrate is taken into account.

Finally, it is remarked that the proposed all-silicon metasurfaces offer the potential for tunable operation through optical excitation of carriers in silicon. The photogenerated conductivity could drastically modify the response of the metasurfaces, for instance, by quenching high-quality factor resonances or disturbing critical coupling conditions,^[57] thus boosting their utility as functional components in real-world applications.

5. Conclusions

To sum up, we demonstrate a not yet explored path toward the experimental realization of dielectric metasurfaces with strong toroidal response at sub-THz frequencies. The technique is based on standard, low-cost microfabrication technology, offering the following advantages: i) definition of the metasurface elements with a single photolithographic step, ii) fabrication by means of a single, self-stopping silicon etching process, iii) involvement of a single silicon wafer without need for additional substrates or host materials, iv) resulting components, which are compact, planar, and self-supported mechanically, and v) potential for tunable operation via, for instance, carrier photogeneration. Both theoretical and experimental investigation has been carried out, confirming the toroidal dipole nature of the resonance manifested by the metasurface in the millimeter-wave W-band. This first demonstration paves the way for the design of all-silicon metasurfaces for the study of toroidal dipole modes or for the engineering of compact components with sharp resonances in the microwave and terahertz spectrum with an eye on next-generation wireless networks, satellite links, and radar applications.

Acknowledgements

This work was supported by the European Union COST Action CA16220 “European Network for High Performance Integrated Microwave Photonics,” by the Comunidad de Madrid and FEDER Program under grant S2018/NMT-4326, the Ministerio de Economía y Competitividad of Spain (TEC2013-47342-C2-2-R), and the mobility programs of Carlos III University and “José Castillejo” of the Ministerio de Educación, Cultura y Deporte of Spain.

Conflict of Interest

The authors declare no conflict of interest.

Keywords

dielectric metasurfaces, microwave wireless components, scattering, toroidal resonances

Received: May 9, 2019
Revised: June 21, 2019
Published online: July 11, 2019

- [1] H.-T. Chen, A. J. Taylor, N. Yu, *Rep. Prog. Phys.* **2016**, 79, 076401.
[2] P. Genevet, F. Capasso, F. Aieta, M. Khorasaninejad, R. Devlin, *Optica* **2017**, 4, 139.
[3] F. Ding, A. Pors, S. I. Bozhevolnyi, *Rep. Prog. Phys.* **2017**, 81, 026401.
[4] S. M. Kamali, E. Arbabi, A. Arbabi, A. Faraon, *Nanophotonics* **2018**, 7, 1041.
[5] R. Paniagua-Domínguez, Y. F. Yu, A. E. Miroshnichenko, L. A. Krivitsky, Y. H. Fu, V. Valuckas, L. Gonzaga, Y. T. Toh, A. Y. S. Kay, B. Luk'yanchuk, A. I. Kuznetsov, *Nat. Commun.* **2016**, 7, 10362.
[6] J. Algorri, B. García-Cámara, A. Cuadrado, J. Sánchez-Pena, R. Vergaz, *Nanomaterials* **2017**, 7, 177.
[7] N. M. Estakhri, V. Nader, M. W. Knight, A. Polman, A. Alù, *ACS Photonics* **2017**, 4, 228.
[8] A. E. Minovich, A. V. Zayats, *ACS Photonics* **2018**, 5, 1755.
[9] E. Arbabi, A. Arbabi, S. M. Kamali, Y. Horie, A. Faraon, *Optica* **2016**, 3, 628.
[10] S. Liu, A. Vaskin, S. Addamane, B. Leung, M.-C. Tsai, Y. Yang, P. P. Vabishchevich, G. A. Keeler, G. Wang, X. He, Y. Kim, N. F. Hartmann, H. Htoon, S. K. Doorn, M. Zilk, T. Pertsch, G. Balakrishnan, M. B. Sinclair, I. Staude, I. Brener, *Nano Lett.* **2018**, 18, 6906.
[11] J. Bohn, T. Bucher, K. E. Chong, A. Komar, D.-Y. Choi, D. N. Neshev, Y. S. Kivshar, T. Pertsch, I. Staude, *Nano Lett.* **2018**, 18, 3461.
[12] S. Yuan, X. Qiu, C. Cui, L. Zhu, Y. Wang, Y. Li, J. Song, Q. Huang, J. Xia, *ACS Nano* **2017**, 11, 10704.
[13] A. Ferraro, D. C. Zografopoulos, M. A. Verschuuren, D. K. G. de Boer, F. Kong, H. P. Urbach, R. Beccherelli, R. Caputo, *ACS Appl. Mater. Interfaces* **2018**, 10, 24750.
[14] A. Arbabi, Y. Horie, M. Bagheri, A. Faraon, *Nat. Nanotechnol.* **2015**, 10, 937.
[15] S. Kruk, B. Hopkins, I. I. Kravchenko, A. Miroshnichenko, D. N. Neshev, Y. S. Kivshar, *APL Photonics* **2016**, 1, 030801.
[16] E. Arbabi, S. M. Kamali, A. Arbabi, A. Faraon, *ACS Photonics* **2018**, 5, 3132.
[17] K. Ou, G. Li, T. Li, H. Yang, F. Yu, J. Chen, Z. Zhao, G. Cao, G. X. Chen, W. Lu, *Nanoscale* **2018**, 10, 19154.
[18] Y. Yang, I. I. Kravchenko, D. P. Briggs, J. Valentine, *Nat. Commun.* **2014**, 5, 5753.
[19] S. Campione, S. Liu, L. I. Babilio, L. K. Warne, W. L. Langston, T. S. Luk, J. R. Wendt, J. L. Reno, G. A. Keeler, I. Brener, M. B. Sinclair, *ACS Photonics* **2016**, 3, 2362.
[20] S. Liu, M. B. Sinclair, S. Saravi, G. A. Keeler, Y. Yang, J. Reno, G. M. Peake, F. Setzpfandt, I. Staude, T. Pertsch, I. Brener, *Nano Lett.* **2016**, 16, 5426.
[21] P. P. Vabishchevich, S. Liu, M. B. Sinclair, G. A. Keeler, G. M. Peake, I. Brener, *ACS Photonics* **2018**, 5, 1685.
[22] A. E. Miroshnichenko, A. B. Evlyukhin, Y. F. Yu, R. M. Bakker, A. Chipouline, A. I. Kuznetsov, B. Luk'yanchuk, B. N. Chichkov, Y. S. Kivshar, *Nat. Commun.* **2015**, 6, 8069.
[23] I. B. Zel'dovich, *J. Exp. Theor. Phys.* **1957**, 1184.
[24] W. C. Haxton, *Science* **1997**, 275, 1753.
[25] C. M. Ho, R. J. Scherrer, *Phys. Lett. B* **2013**, 722, 341.
[26] N. Talebi, S. Guo, P. A. van Aken, *Nanophotonics* **2017**, 7, 93.
[27] A. I. Kuznetsov, A. E. Miroshnichenko, M. L. Brongersma, Y. S. Kivshar, B. Luk'yanchuk, *Science* **2016**, 354, aag2472.
[28] A. C. Tasolamprou, O. Tsilipakos, M. Kafesaki, C. M. Soukoulis, E. E. Economou, *Phys. Rev. B* **2016**, 94, 205433.
[29] A. K. Ospanova, G. Labate, L. Matekovits, A. A. Basharin, *Sci. Rep.* **2018**, 8, 12514.
[30] R. Wang, L. D. Negro, *Opt. Express* **2016**, 24, 19048.
[31] J. S. T. Gongora, A. E. Miroshnichenko, Y. S. Kivshar, A. Fratallocchi, *Nat. Commun.* **2017**, 8, 15535.
[32] N. A. Nemkov, I. V. Stenishchev, A. A. Basharin, *Sci. Rep.* **2017**, 7, 1064.
[33] G. Grinblat, Y. Li, M. P. Nielsen, R. F. Oulton, S. A. Maier, *ACS Nano* **2016**, 11, 953.
[34] M. Timofeeva, L. Lang, F. Timpu, C. Renaut, A. Bouravleuv, I. Shtrom, G. Cirlin, R. Grange, *Nano Lett.* **2018**, 18, 3695.
[35] V. R. Tuz, V. V. Khardikov, Y. S. Kivshar, *ACS Photonics* **2018**, 5, 1871.
[36] Y. He, G. Guo, T. Feng, Y. Xu, A. E. Miroshnichenko, *Phys. Rev. B* **2018**, 98, 161112.
[37] O. Tsilipakos, A. C. Tasolamprou, T. Koschny, M. Kafesaki, E. N. Economou, C. M. Soukoulis, *Adv. Opt. Mater.* **2018**, 6, 1800633.

- [38] S. Lepeshov, Y. Kivshar, *ACS Photonics* **2018**, *5*, 2888.
- [39] A. A. Basharin, V. Chuguevsky, N. Volsky, M. Kafesaki, E. N. Economou, *Phys. Rev. B* **2017**, *95*, 035104.
- [40] S.-D. Liu, Z. X. Wang, W. J. Wang, J. D. Chen, Z. H. Chen, *Opt. Express* **2017**, *25*, 22375.
- [41] J. Algorri, D. C. Zografopoulos, A. Ferraro, B. García-Cámara, R. Vergaz, R. Beccherelli, J. Sánchez-Pena, *Nanomaterials* **2019**, *9*, 30.
- [42] J. Algorri, D. C. Zografopoulos, A. Ferraro, B. García-Cámara, R. Beccherelli, J. Sánchez-Pena, *Opt. Express* **2019**, *27*, 6320.
- [43] I. V. Stenishchev, A. A. Basharin, *Sci. Rep.* **2017**, *7*, 9468.
- [44] A. Sayanskiy, M. Danaeifar, P. Kapitanova, A. E. Miroshnichenko, *Adv. Opt. Mater.* **2018**, *6*, 1800302.
- [45] S. Xu, A. Sayanskiy, A. S. Kupriianov, V. R. Tuz, P. Kapitanova, H. B. Sun, W. Han, Y. S. Kivshar, *Adv. Opt. Mater.* **2019**, *7*, 1801166.
- [46] D. C. Zografopoulos, J. F. Algorri, A. Ferraro, B. García-Cámara, J. M. Sánchez-Pena, R. Beccherelli, *Sci. Rep.* **2019**, *9*, 7544.
- [47] Y. Yang, W. Wang, A. Boulesbaa, I. I. Kravchenko, D. P. Briggs, A. Poretzky, D. Geohegan, J. Valentine, *Nano Lett.* **2015**, *15*, 7388.
- [48] P. Pal, K. A. Sato, *Micro Nano Syst. Lett.* **2015**, *3*, 6.
- [49] G. Dayal, X. Y. Chin, C. Soci, R. Singh, *Adv. Opt. Mater.* **2016**, *4*, 1860.
- [50] J. Krupka, P. Kaminski, L. Jensen, *IEEE Trans. Microwave Theory Tech.* **2016**, *64*, 4149.
- [51] D. C. Zografopoulos, E. E. Kriezis, B. Bellini, R. Beccherelli, *Opt. Express* **2007**, *15*, 1832.
- [52] M. Albooyeh, D. Morits, S. A. Tretyakov, *Phys. Rev. B* **2012**, *85*, 205110.
- [53] M. Mayer, M. Tebbe, C. Kuttner, M. J. Schnepf, T. A. F. König, A. Fery, *Faraday Discuss.* **2016**, *191*, 159.
- [54] P. Gutruf, C. Zou, W. Withayachumnankul, M. Bhaskaran, S. Sriram, C. Fumeaux, *ACS Nano* **2015**, *10*, 133.
- [55] T. Xu, Z. Tao, H. Li, X. Tan, H. Li, *Adv. Mech. Eng.* **2017**, *9*, 1.
- [56] Silicon wafers by Silicon Materials, <https://www.si-mat.com/> (accessed: June 2019).
- [57] K. Fan, J. Zhang, X. Liu, G. F. Zhang, R. D. Averitt, W. J. Padilla, *Adv. Mater.* **2018**, *30*, 1800278.